A&A 553, A54 (2013)
DOI: 10.1051/0004-6361/201220894

Astronomy & Astrophysics

Statistical studies of HII regions in nearby galaxies

I. *Spitzer* near-IR luminosities and temperatures, compared with Hα luminosities, from selected HII regions in M100

S. J. Chan[1,2] and J. E. Beckman[2,3,4]

[1] 43 Tamar Way, Didcot, OX11 7QH, UK
e-mail: sjchan2012@gmail.com
[2] Instituto de Astrofisica de Canarias, 38205 La Laguna, Spain
e-mail: jeb@iac.es
[3] CSIC, 28006 Madrid, Spain
[4] Department of Astrophysics, University of La Laguna, 38200 La Laguna, Tenerife, Spain

Received 12 December 2012 / Accepted 27 February 2013

ABSTRACT

Aims. We systematically study the relations between the Hα luminosity and the near-IR luminosity and temperature of a set of selected HII regions in the disc of M100.
Methods. By using the technique of cross-reference between the optical Hα image (the catalogue of HII regions in M100) and the *Spitzer* IRAC images, we locate the selected HII regions in the IRAC image frames. By using the chi-squared non-linear fitting technique, we estimate the IRAC-3-band colour temperature $T_{\rm col(IRAC)}$ of selected HII regions, and calculate their near-IR luminosities.
Results. The spectral fits allow us to separate the PAH emission in the 3.6 μm band from the thermal dust emission that dominates the other three bands, thereby assigning values for the colour temperature of the dust. These values lie in the range 250 K to 350 K. There is a well defined linear relation between the Hα luminosity and the derived IRAC luminosity for the HII regions, but no apparent relation between the latter and the colour temperature. While the range in Hα luminosity is almost two orders of magnitude, the range in temperature is less than a factor two. We also find that the colour temperature is independent of galactocentric radius, in contrast to previous findings for electron temperatures in HII regions. These results could be understood in scenarios where the OB association pushes the surrounding dust and gas out to radii that are larger for higher luminosity regions or, alternatively, where the dust we are measuring consists of tiny stochastically heated grains.

Key words. galaxies: individual: M 100 – galaxies: ISM – HII regions – infrared: galaxies – methods: statistical – infrared: ISM

1. Introduction

The statistical properties of HII regions in galaxies have been extensively studied since the 1970s (see e.g., Hodge 1976; Kennicutt 1984; Kennicutt et al. 1989; Rozas et al. 1996). These studies, largely via observations of hydrogen recombination lines, provide important clues to the physics of massive star formation. The addition of infrared observations provides insight into those processes that connect star formation to the interstellar medium, and is an additional tool for studying star formation itself. Well-resolved infrared space observations of nearby galaxies are allowing us to apply data with excellent sensitivity and satisfactory angular resolution, which can be matched to their ground-based optical counterparts.

Following the pioneering space-based IRAS infrared survey (Beichman et al. 1988) and the second generation of measurements with ISO (Kessler et al. 1996), the *Spitzer* Space Telescope (Werner et al. 2004, hereinafter called simply *Spitzer*) has allowed, and continues to allow, astronomers to survey the thermal emission radiated individual infrared sources in nearby galaxies via its three operational instruments, the Infrared Array Camera (IRAC, Fazio et al. 2004), the Multiband Imaging Photometer for *Spitzer* (MIPS), and the Infrared Spectrometer, IRS. The *Spitzer* Infrared Nearby Galaxies Survey (SINGS, Kennicutt et al. 2003) is a comprehensive infrared imaging and spectroscopic survey of 75 galaxies within 30 Mpc, designed to probe the full range of star-forming environments and to provide a heritage archive. The pixel scale of the SINGS-IRAC mosaic images has been refined to 0.75 arcsec/pixel by the SINGS team, based on an original scale of 1.2 arsec/pixel.

The project, for which this is the pilot study, is designed to take advantage of the SINGS archive images. We chose M100 for this study because it has been deeply studied, and we were able to use a comprehensive survey of its HII regions as recorded in Knapen (1998), as well as an Hα image from (Knapen et al. 2004). M100 (NGC 4321) is a grand-design galaxy of class .SXS4 (De Vaucouleurs et al. 1991), with a fairly weak major bar. It is a very well defined spiral, class 12 in the scheme of (Elmegreen & Elmegreen 1987), with arms ranging between 15 arcsec and 150 arcsec from the nucleus. It has an inner bar and a star-forming ring in the circumnuclear region (Knapen et al. 1995a,b). We use the distance obtained in the HST key programme, using Cepheids, of 14.3 Mpc (Freedman et al. 2001).

One of the primary goals here is to compare the infrared luminosity of the HII regions of M100 with that in Hα emission. For this purpose we have used *Spitzer* IRAC data to complement the Hα data of Knapen (1998). In this paper we present an overview and some key initial results. The structure of the

article is as follows. In Sect. 2 we describe the selection of the HII region sample, Section 3 describes the measurement and data analysis, and Sect. 4 gives the results of the analysis. The discussion and summary are in Sects. 5 and 6, respectively.

2. Data and sample

The photometric, image in Hα was taken at the 4.2 m William Herschel Telescope, La Palma (Knapen 1998). The set of HII regions, calibrated in Hα luminosity, and the image in Hα were obtained from the SIMBAD archive. The SINGS/IRAC images of M100 were obtained from the SINGS Public Data Set Archive[1].

2.1. Image in Hα emission, and Hα catalogue

The disc of M100 was sampled with a spatial resolution of 1″ and a pixel scale of 0.24″. Knapen et al. (1998, 2003) selected the HII regions for measurement using the following criteria: a region detected with statistical significance needs to have at least nine contiguous pixels with a surface brightness at least three times greater than the noise level of the local background, and the uncertainty in the determination of the surface brightness should not be affected by more than 10% in the weakest region. Regions from the arms, the interarm region, and the circumnuclear region have all been included in the measurements. The sky background in the original image was very uniform, allowing a constant subtraction value for the whole galaxy (Knapen et al. 2003). The luminosities were obtained by integrating the counts within a circular aperture, whose radius was taken as the mean of the minimum and maximum radial extent of a region (regions in general are not perfectly circular), taken as the effective radius of a region. The estimated uncertainty in the luminosity of a given region is 10% (Knapen 1998).

2.2. Infrared Array Camera (IRAC) images

IRAC (Fazio et al. 2004) is an infrared camera operating simultaneously in four wavelength bands centred on 3.6 μm, 4.5 μm, 5.8 μm, and 8.0 μm. There are four detectors, each sized 256 × 256 pixels; InSb detectors cover the 3.6 μm and 4.5 μm bands, while SiAS IBC detectors cover the 5.8 μm and 8.0 μm bands. The sensitivity limits are 0.92, 1.22, 6, and 9 μJy (1σ, 200 s), respectively, in the four bands. The 1σ sensitivity in μJy is given for the low-background case (near the ecliptic poles). The values were calculated based on the sensitivity model given by (Hora et al. 2000). The reference unit for the IRAC images is MJy sr^{-1} and typical backgrounds in the four bands are 0.15 MJy sr^{-1}, 0.44 MJy sr^{-1}, 2.3 MJy sr^{-1}, and 9.3 MJy sr^{-1}, respectively. The details of the noise level can be seen in the IRAC Pocket Guide (Spitzer's Science Support Team 2006).

2.3. Selection and location of the samples in the IRAC image frames

In the present pilot study we confined our attention to those HII regions with radii between 2.23 arcsec and 4.46 arcsec. We noticed that some of the HII regions with apparently larger radii than our selected upper limit were mergers of more than one region in the IRAC image frames, which have lower angular resolution than our optical data. We also noted that some regions with smaller radii than our lower limit did not have sufficiently well-defined limits. This effect can also be present in Hα and can cause systematic errors (Knapen et al. 2003), and although Zurita et al. (2000) evolved techniques to surmount this difficulty, we deemed it wiser to use the lower limit stated above. The total number of regions initially selected was 80, although we finally had to exclude two of these because they could not be fitted with a single black body temperature.

To locate the HII regions, registering their positions in the Hα image frame and also the IRAC image frames, we needed to transform the coordinate system of the Hα map (hereinafter we refer to the HII regions taken from this map as K-HII regions) from coordinates in arcsec related to the zero position on the nucleus to a pixel system, which we could then use to make the appropriate cross-reference to the IRAC image frames. We used the IRAF task *image.tvmark* to mark the location of each selected K-HII region in the Hα image.

3. Measurements and data analysis

3.1. Alignment of the IRAC images with the Hα image

The input unit of the IRAC images is MJy sr^{-1}, and before we aligned the IRAC image frames with the Hα image frame, we transformed this to μJy pixel^{-1}. The precise alignment process was needed to be sure that no data were lost or wrongly cross-correlated when making our comparison. The procedure used the IRAF task *image.immatch.srgister*. We used the Hα image as the fiducial frame because it has the highest intrinsic resolution. The IRAC images were regridded to give them the same pixel scale as the fiducial frame. They were then rotated, translated, and rescaled so that the final versions are correctly orientated and registered (see Figs. 1a,b).

3.2. Measurement of the K-HII regions in the IRAC bands

The measurement procedure was as follows:

(a) We displayed the Hα image frame and the four IRAC frames (one at a time) in *Ximtool* using the IRAF task *image.display*.
(b) We marked with an *X* each of the selected K-HII regions on the Hα frame and on the IRAC image frame. The pixel values of the K-HII regions are listed in Cols. 2 and 3 (xpos-img, ypos-img) in Table 1. This is done using the IRAF task *image.tvmark*.
(c) The fluxes of the K-HII regions in the IRAC images were measured using the IRAF task *noao.digiphot.appphot.phot*.
(d) The fluxes were determined by integrating in a circular aperture around the centres of the regions.
(e) The local sky background was subtracted from the measured fluxes to give the final values of the flux measurements. The median relative uncertainties of the measured fluxes were 4.5% in the 3.6 μm band, 5.1% in the 4.5 μm band, 2.2% in the 5.8 μm band, and 1.4% in the 8.0 μm band. These values are consistent with the reported values of about 5% for typical observers (see Spitzer Science Center 2006). In one outlying case (K-HII region 1008) we do find much higher uncertainties (19%, 21%, 10%, and 7% in the four bands, respectively).

3.3. Colour and aperture corrections

According to the IRAC Data Handbook (Spitzer Science Center 2006), it is necessary to apply colour correction and aperture correction for better results, and we proceeded to apply both of

[1] http://sings.stsci.edu/

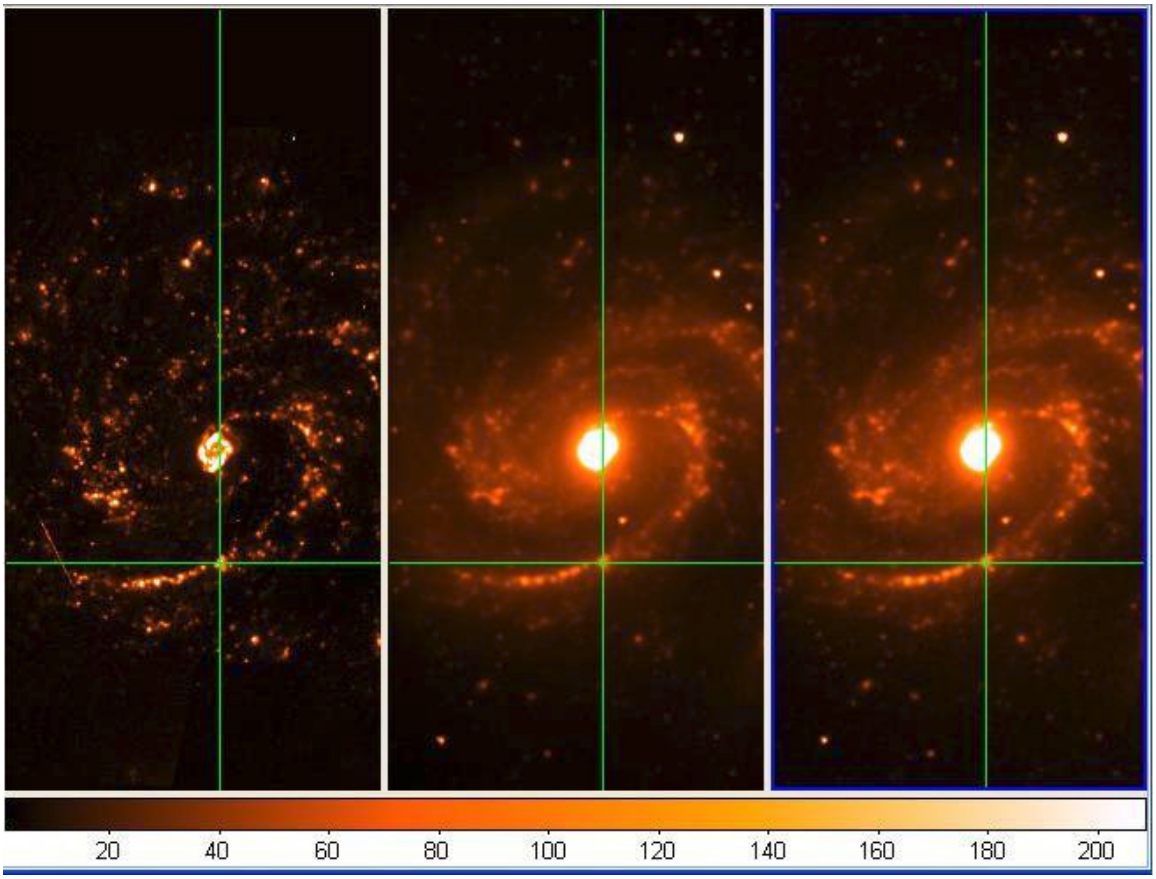

Fig. 1. a) Aligned images, *left to right*: Hα image, IRAC 3.6 μm image, IRAC 4.5 μm image.

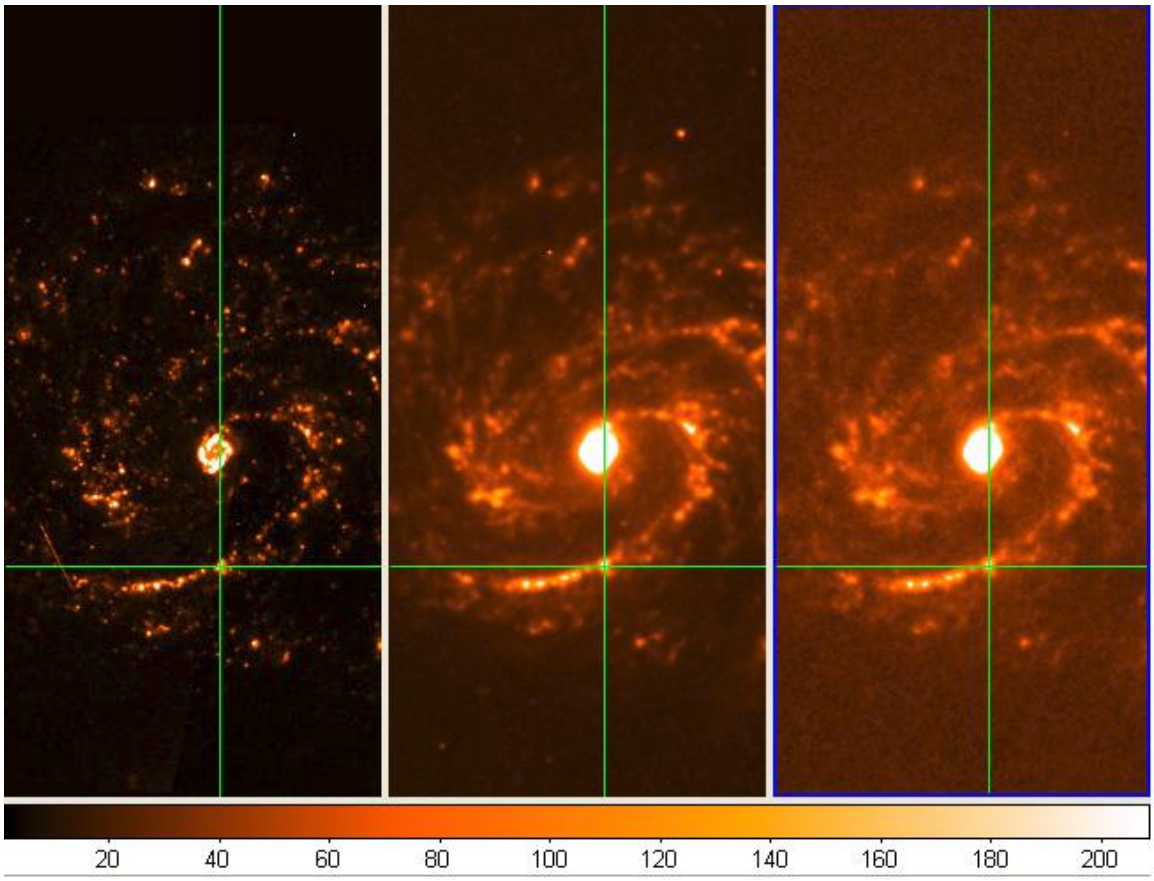

Fig. 1. b) Aligned images, *left to right*: Hα image, IRAC 5.6 μm image, IRAC 8.0 μm image.

Table 1. Measured IRAC fluexes of selected K-HII regions.

K-HII	xpos-img	ypos-img	IRAC fluxes (μJy)				Relative uncertainties (%)			
	(pix)	(pix)	3.6 μm	4.5 μm	5.6 μm	8.0 μm	3.6 μm	4.5 μm	5.8 μm	8.0 μm
0047	694.280	1409.670	23.4	16.5	88.2	257.8	11.5	12.9	5.6	3.3
0091	791.370	855.810	69.1	44.9	139.6	427.1	6.7	7.9	4.5	2.6
0182	908.010	1507.970	114.7	97.1	522.5	1391.6	5.3	5.3	2.5	1.8
0196	916.970	1470.710	111.6	88.2	547.5	1519.7	5.3	5.5	2.3	1.6
0238	957.600	1138.590	511.5	416.7	2268.7	6662.6	2.5	2.6	1.1	0.7
0352	1034.110	1541.370	77.1	56.9	296.7	888.0	6.4	7.0	3.0	1.8
0396	1052.740	1205.480	323.5	256.6	1229.9	3562.7	3.2	3.4	1.7	1.2
0462	1076.190	1018.800	373.8	301.2	1613.5	4543.3	3.1	3.2	1.6	1.1
0493	1088.920	1092.990	213.9	187.0	963.3	2589.7	4.0	4.0	1.7	1.1
0504	1094.400	829.590	279.9	194.8	1064.2	3170.0	3.4	3.8	1.7	1.0
0517	1099.460	982.160	58.9	39.1	379.7	1159.7	10.9	11.6	3.5	2.5
0546	1114.030	995.730	88.8	56.5	207.5	624.6	7.8	8.6	5.2	4.1
0585	1131.870	833.780	817.2	641.4	3260.7	8793.7	1.9	2.0	0.9	0.6
0623	1152.120	733.610	142.3	111.8	683.4	1940.6	4.8	5.1	2.1	1.3
0639	1159.420	1739.170	421.5	321.8	1743.6	4981.7	2.7	2.9	1.3	0.7
0651	1167.680	839.130	932.0	781.6	4326.3	11971.6	1.8	1.8	0.8	0.5
0681	1189.380	742.580	119.7	80.5	525.6	1560.3	5.4	6.1	2.4	1.4
0702	1201.540	842.910	365.2	288.3	1424.7	3940.7	2.9	3.1	1.4	0.8
0733	1218.140	1714.240	92.6	62.8	327.3	942.0	5.7	6.5	2.9	1.8
0737	1218.630	857.140	628.2	509.6	2754.6	7566.2	2.2	2.3	1.0	0.6
0740	1219.210	836.930	711.1	574.5	3132.9	8915.6	2.1	2.2	0.9	0.6
0763	1232.160	1562.490	335.0	286.2	1151.0	3078.9	3.0	3.1	1.6	1.0
0788	1243.450	746.930	84.5	47.8	336.7	962.6	6.3	7.6	2.9	1.7
0818	1260.710	1603.990	258.6	200.5	1107.9	3139.8	3.4	3.7	1.6	0.9
0846	1272.700	873.320	537.0	398.0	1958.9	5850.3	2.4	2.6	1.2	0.7
0870	1281.080	1588.010	69.3	52.2	254.5	726.5	6.7	7.4	3.4	2.2
0885	1286.100	1734.650	55.9	52.4	236.2	591.8	7.4	7.2	3.4	2.2
0921	1300.790	1170.380	3597.6	1563.2	5985.2	18315.5	0.9	1.6	0.7	0.5
0945	1308.590	1398.100	58.8	36.9	383.4	580.5	7.6	9.0	3.1	3.0
0953	1311.990	880.670	1681.6	1337.2	7439.9	20982.7	1.4	1.5	0.6	0.4
0963	1314.360	1086.100	1614.7	1180.3	4095.3	18584.8	1.4	1.6	0.8	0.4
0991	1324.440	1452.780	159.0	109.4	466.8	1536.5	4.5	5.1	2.9	1.3
1008	1331.500	668.800	10.3	6.8	40.0	119.7	19.2	21.5	10.5	6.6
1026	1339.750	895.110	201.8	151.0	746.2	2210.6	4.1	4.3	1.9	1.3
1033	1340.380	735.480	37.0	24.9	149.5	387.9	9.2	10.6	4.3	2.8
1039	1344.110	910.750	199.5	110.7	636.3	1887.3	4.1	5.1	2.2	1.8
1085	1361.580	1410.130	89.2	70.3	363.1	1086.5	6.0	6.4	2.9	2.0
1092	1364.190	1079.170	153.5	111.6	511.6	1405.8	4.6	5.2	2.9	2.3
1149	1391.120	706.270	307.0	256.2	1275.2	3431.2	3.1	3.2	1.5	0.9
1158	1395.020	1220.210	130.2	94.7	560.1	1548.0	5.7	6.1	2.7	2.0
1162	1399.170	943.280	118.4	97.9	603.1	1834.6	5.3	5.3	2.1	1.2
1166	1402.700	1751.460	185.5	141.3	533.4	1530.8	4.1	4.4	2.3	1.4
1195	1411.160	1433.120	31.8	22.3	151.6	540.9	15.0	15.3	6.2	4.3
1222	1421.370	924.570	101.2	61.9	326.8	965.1	6.4	7.5	3.7	2.4
1244	1432.040	1216.230	267.8	281.0	1437.4	4111.5	3.6	3.1	1.4	0.8
1247	1434.030	911.370	108.2	63.4	324.6	956.3	6.2	7.4	3.7	2.5
1264	1442.240	1429.170	76.7	72.0	198.4	444.8	7.3	6.7	4.1	3.3
1300	1460.290	680.380	156.3	105.9	451.0	1224.2	4.4	5.1	2.5	1.6
1324	1470.330	1677.430	99.8	69.3	356.0	989.7	5.6	6.4	2.8	1.7
1343	1479.010	993.200	470.9	378.2	1948.8	5325.8	2.8	2.9	1.3	0.8
1349	1480.090	1260.790	141.4	89.1	324.3	935.9	5.1	5.9	3.9	3.4
1368	1489.090	1235.360	339.8	274.2	1269.4	3571.3	3.2	3.2	1.5	0.9
1369	1489.130	1589.760	64.0	55.8	397.0	1116.9	7.1	7.1	2.6	1.6
1377	1491.910	1406.060	134.8	98.0	623.0	1848.2	4.9	5.3	2.1	1.2
1394	1499.300	1017.430	306.1	219.8	1204.0	3572.3	3.9	4.1	1.8	1.4
1409	1506.100	1079.840	230.6	182.0	864.3	2546.7	4.1	4.1	1.8	1.1
1416	1508.220	1184.200	742.5	618.4	3106.5	8618.8	2.1	2.1	0.9	0.6
1419	1510.420	1235.730	437.2	303.3	1322.7	2765.7	3.0	3.3	1.6	1.3
1433	1515.980	1408.260	147.3	118.3	571.2	1736.3	4.8	5.0	2.3	1.5
1454	1526.140	1097.020	270.7	177.8	1006.5	2960.3	4.0	4.4	2.0	1.6
1511	1549.090	1257.390	111.0	82.4	311.0	849.2	5.4	5.9	3.7	3.0
1566	1577.260	1104.320	191.3	135.5	630.2	1762.7	4.1	4.6	2.0	1.2
1567	1578.090	1015.560	71.0	53.5	264.8	765.6	6.6	7.2	3.4	2.0
1574	1581.910	1163.280	202.3	168.6	739.6	1995.2	4.0	4.1	2.0	1.4
1610	1602.240	1269.010	74.9	55.0	335.2	980.4	6.4	7.1	2.9	2.0

Table 1. continued.

K-HII	xpos-img (pix)	ypos-img (pix)	IRAC fluxes (μJy) 3.6 μm	4.5 μm	5.6 μm	8.0 μm	Relative uncertainties (%) 3.6 μm	4.5 μm	5.8 μm	8.0 μm
1625	1616.850	1364.110	92.2	65.5	506.8	1620.0	6.1	6.7	3.1	2.4
1650	1636.310	1413.280	148.5	102.1	696.9	2415.0	5.4	6.0	2.3	1.1
1667	1651.120	1352.410	471.7	382.2	2167.1	6191.0	2.9	2.9	1.1	0.7
1674	1657.060	1300.380	167.8	147.6	722.3	2029.2	4.4	4.4	2.2	1.7
1708	1674.440	705.320	227.0	170.9	881.2	2420.5	3.7	4.0	1.8	1.1
1772	1725.690	748.050	90.6	75.6	458.3	1255.5	5.8	6.0	2.5	1.6
1810	1744.480	1236.520	469.4	463.2	2202.4	6016.1	2.7	2.4	1.1	0.6
1837	1765.440	1188.550	554.5	480.8	2506.9	6831.5	2.4	2.4	1.1	0.8
1874	1801.990	954.650	140.9	99.2	605.1	1826.6	4.7	5.3	2.1	1.3
1882	1807.100	927.640	410.5	308.3	1573.3	4503.2	2.8	2.9	1.4	0.8
1891	1814.110	1054.980	73.3	48.7	315.5	936.8	6.5	7.6	3.0	1.8
1922	1834.770	1279.590	32.3	24.0	122.4	342.2	10.0	11.0	4.9	3.0
1928	1840.040	1066.230	258.9	207.8	1245.3	3962.7	3.8	3.9	1.9	1.2

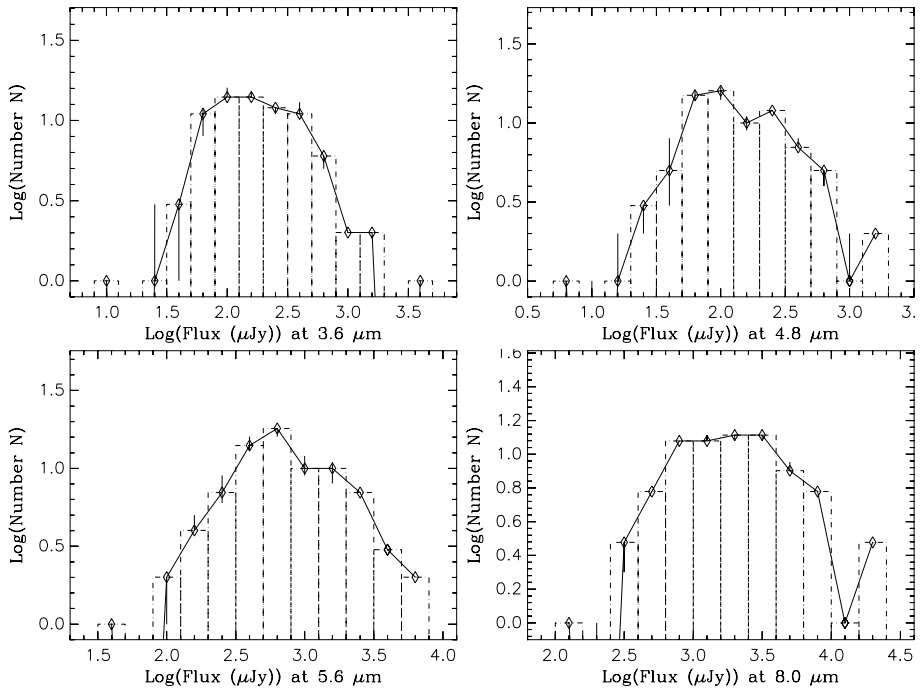

Fig. 2. a) Histograms of the IRAC fluxes for the K-HII regions of M100 in the four IRAC bands.

these, as well as to perform the error tracking calculations related to the corrections.

3.3.1. Colour correction

The IRAC Data Handbook (Spitzer Science Center 2006) gives a recipe for interpreting the data from sources with spectral shapes different from the nominal shape assumed in the standard calibration procedure. If the energy distribution in flux per octave is not constant, it is advisable to apply the colour correction to the quoted flux densities. The convention used for IRAC is the same as for IRAS (Beichman et al. 1988) and ISO (Blommaert et al. 2003). We applied the colour correction as prescribed in the IRAC Data Handbook.

3.3.2. Aperture correction

The IRAC data are calibrated using aperture photometry on a set of selected stars. The calibration aperture has a radius of ten original ("*native*") pixels, 12.2 arcsec, in all four channels. A much smaller on-source aperture is needed for crowded fields. In the presence of extended emission, a small off-source annulus is normally used. The calibration aperture does not take in all the light from the calibration sources, so the extended emission appears too bright in the data products delivered initially (Spitzer Science Center 2006). We first applied the aperture correction to the colour-corrected fluxes using the method described in the IRAC Data Handbook (Spitzer Science Center 2006, see Table 5.7). We then went on to compare the results to the uncorrected values to test whether there was a significant difference. Figure 2 shows the histogram of the IRAC measured fluxes, both corrected and uncorrected, in all four bands.

4. Results

4.1. Estimation of colour temperatures $T_{\mathrm{col(IRAC)}}$ using three bands

When we examined the spectral energy distribution (SED) of a typical K-HII region in the four IRAC bands, we noted that it is possible to fit a black body curve well to the fluxes in the 4.5 μm, 5.8 μm, and 8.0 μm bands (hereinafter the upper three IRAC bands), while the 3.6 μm flux is clearly present in excess.

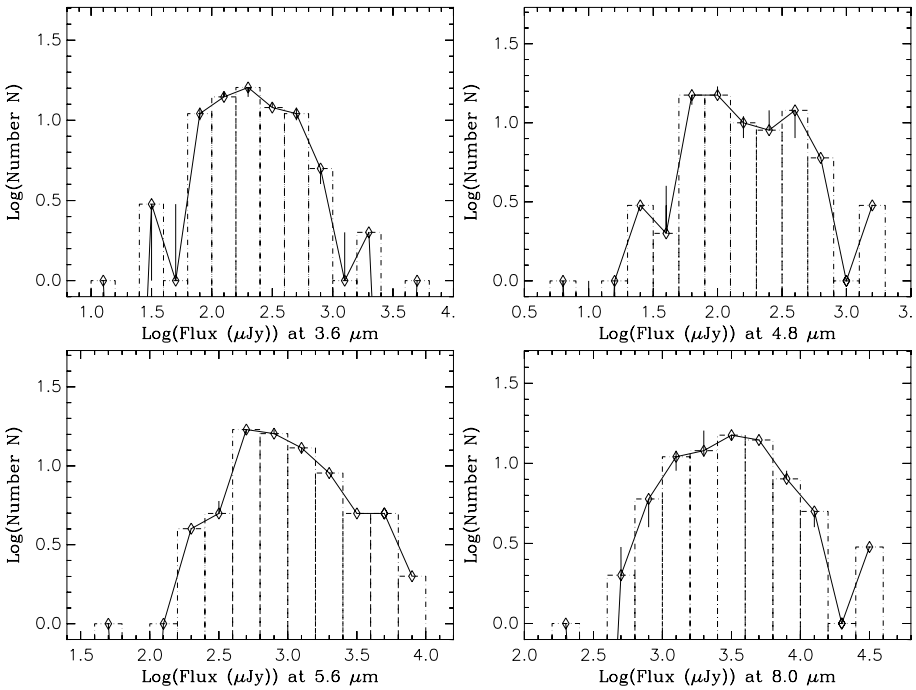

Fig. 2. b) Histograms of the colour+aperture-corrected IRAC fluxes in the four IRAC bands.

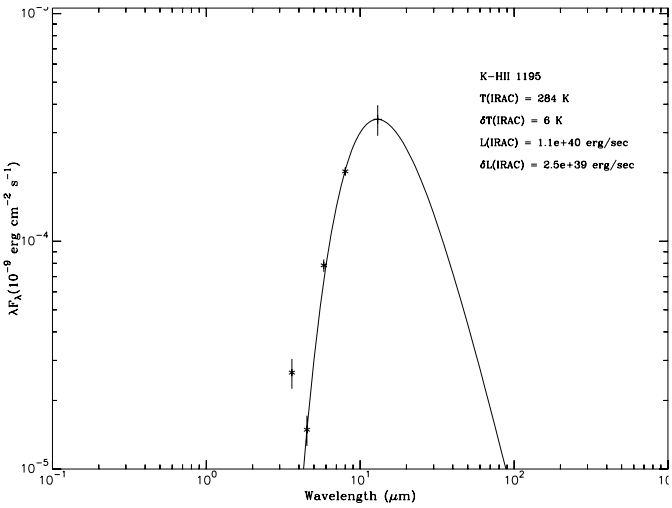

Fig. 3. a) The IRAC fluxes of a representative HII region (K-HII 1195) for the four bands, with a best black body fit to the three longer wavelength bands. The point at the maximum of the curve is not an observed flux, but the estimated peak flux with its error bar. Also the 3.6 μm flux shows a marked excess over the black body curve.

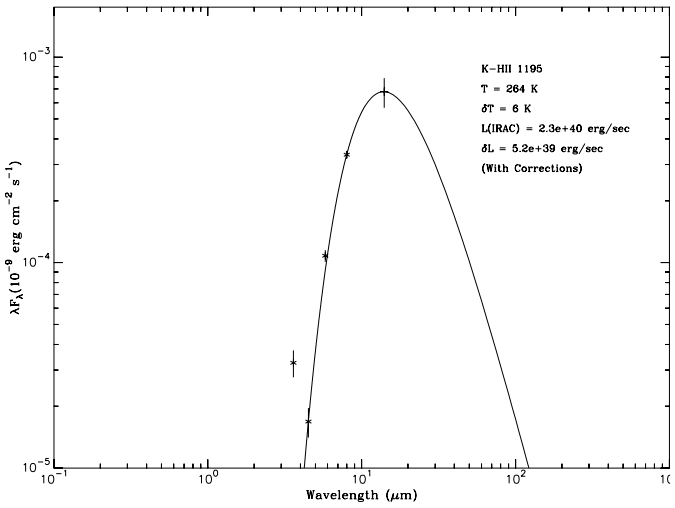

Fig. 3. b) The same as Fig 3a, but with colour+aperture-corrected fluxes.

We refer to the literature in Sect. 5.3 to identify the source of this excess. We could infer a colour temperature, $T_{\rm col(IRAC)}$, from the fluxes in the three upper bands, which we measured for each region. We made this estimate using a chi-squared black body fit to the measured fluxes and colour+aperture-corrected fluxes.

Figure 3 shows the black body fit to a representative K-HII region (K-HII 1195), using both the uncorrected and colour+aperture-corrected fluxes (herineafter called corrected fluxes). The best fits yield temperatures, $T_{\rm col(IRAC)}$, of 284 K without correction, and 264 K with corrections. We found by inspection that the fits to our spectra made using corrected fluxes are slightly better than those made using the uncorrected fluxes. We also present the black body fits using corrected fluxes for a set of sampled K-HII regions in Fig. 4[2].

One of the main results of the present article is the set of $T_{\rm col(IRAC)}$ values for the selected set of K-HII regions (see Sect. 2.3 for the criteria), and in Fig. 5 we present these results as a histogram. We can see that the mode value is 310 K, with a range from 260 to 360 K for the measurements made with uncorrected fluxes (Fig. 5a), while for the measurements with corrected fluxes the mode is 290 K, with a range from 240 K to 340 K (Fig. 5b). The difference in $T_{\rm col(IRAC)}$ for the two cases is of order 20 K, with the uncorrected fluxes giving the higher set of values (see Figs. 3 and 5). This range of colour temperatures, which can also be seen in Fig. 6, is surprisingly restricted given the range of luminosities of the regions: some two orders of magnitude in either Hα or IR luminosity (see also Figs. 6 and 7).

[2] All the fitting plots are available from the authors on request.

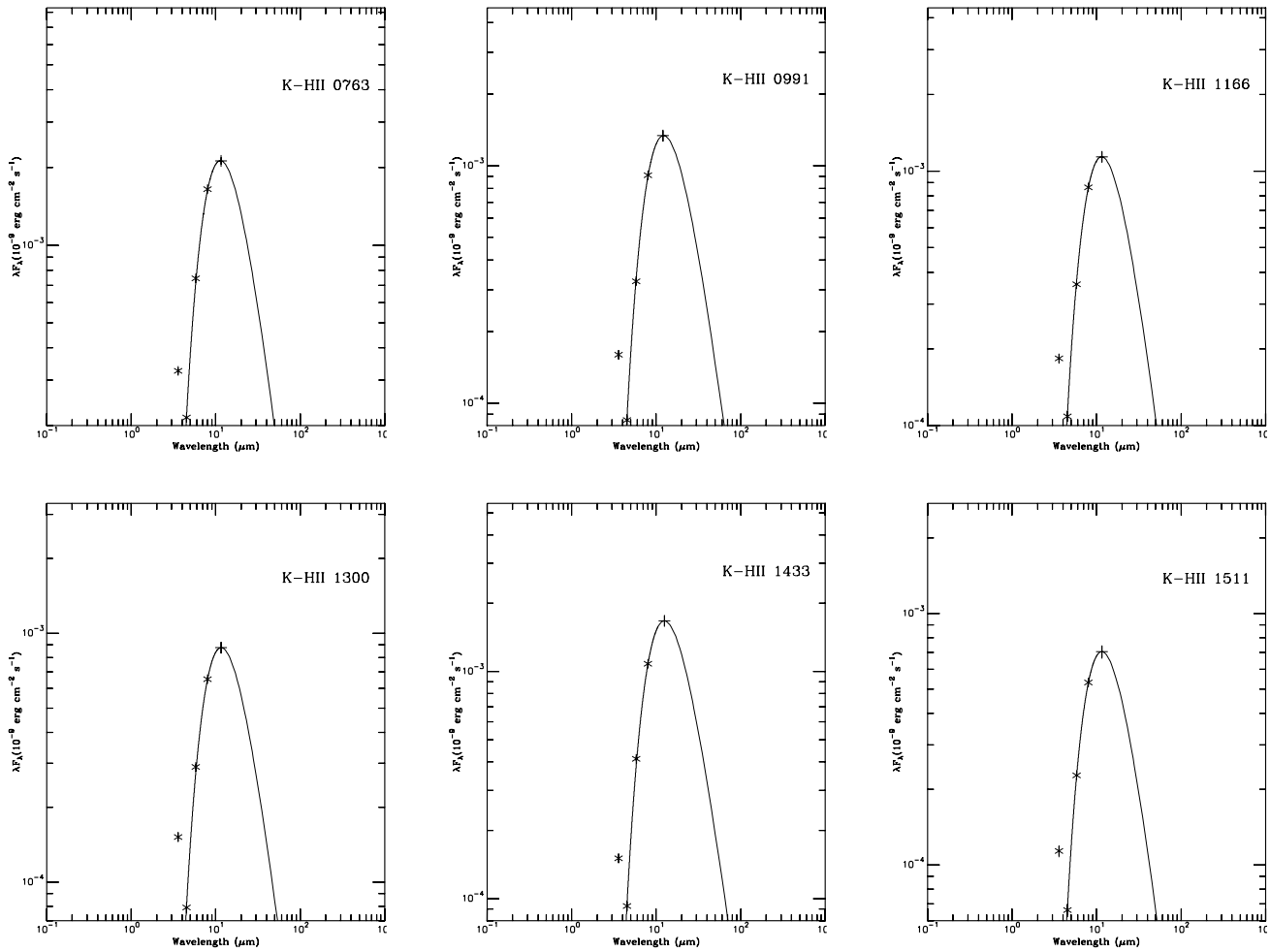

Fig. 4. The same as Fig. 3b, but with a sample of selected HII regions.

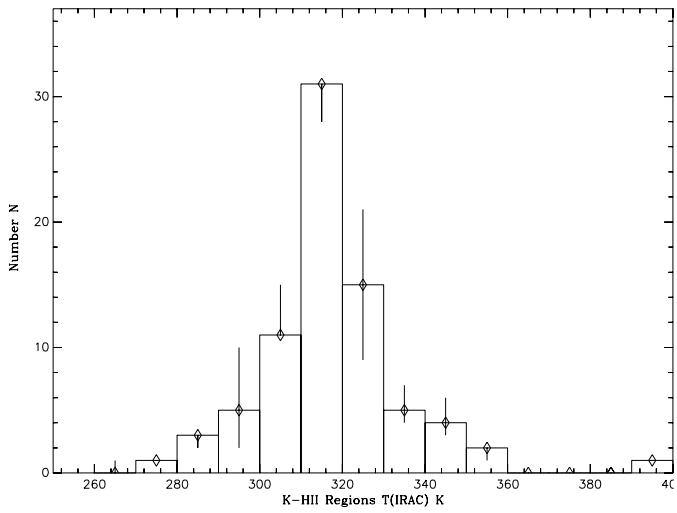

Fig. 5. a) Histogram of colour temperature $T_{\rm col(IRAC)}$ for the K-HII regions with measured fluxes in the IRAC bands.

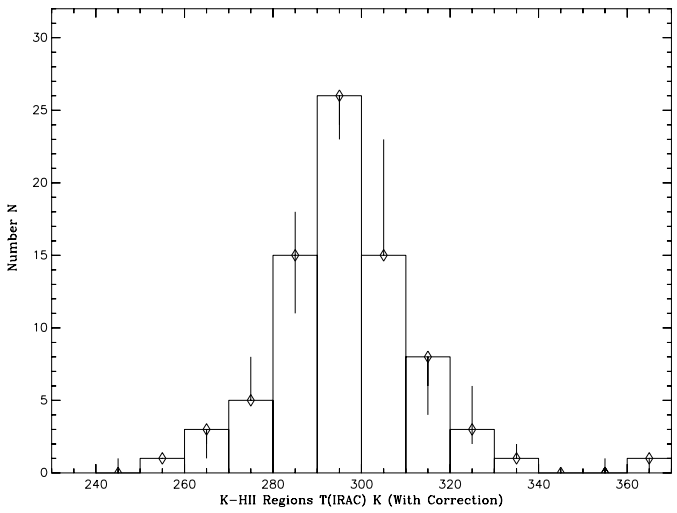

Fig. 5. b) As Fig. 5a but the fluxes here have been subjected to colour+aperture-correction.

4.2. Comparison between the IRAC luminosity, L(IRAC), and the Hα luminosity L(Hα)

4.2.1. Values of L(IRAC), L(Hα) and $T_{\rm col(IRAC)}$

We estimate the IRAC luminosity, L(IRAC), from the angular size of the HII region, its colour temperature and the distance of M100, for which we took 14.3 Mpc (Freedman et al. 2001). In Fig. 6 we plot the Hα luminosity, L(Hα) v. $T_{\rm col(IRAC)}$, using corrected values, while in Fig. 7 we show the equivalent plot of L(IRAC) v. $T_{\rm col(IRAC)}$ (see Table 2). It is clear from Figs. 6 and 7 that there is no functional relationship between $T_{\rm col(IRAC)}$ and either L(IRAC) or L(Hα). The positions of the HII regions within

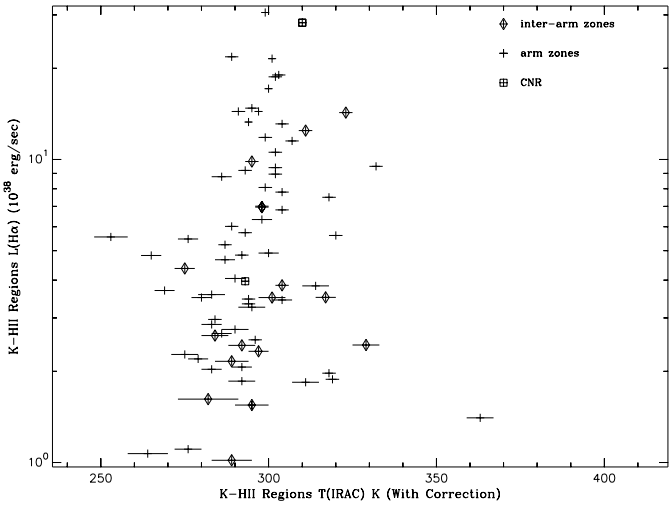

Fig. 6. Colour+aperture-corrected values of the colour temperature $T_{\mathrm{col(IRAC)}}$ against $L(\mathrm{H}\alpha)$ for the K-HII regions sampled with IRAC.

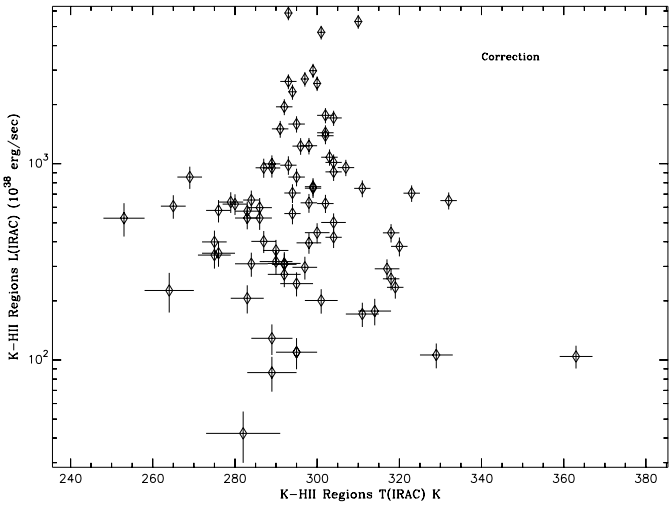

Fig. 7. Colour temperature, $T_{\mathrm{col(IRAC)}}$ as a function of the infrared luminosity L(IRAC) for the HII regions measured, with colour+aperture-corrected values for L(IRAC) and $T_{\mathrm{col(IRAC)}}$.

the galaxy have been indicated by using separate symbols (see Fig. 6). There is no evidence in Figs. 6 and 7, of any differences in the relations between the luminosities and the IR temperature, of any kind, between these differently placed HII regions. Although there appears to be a convergence towards high luminosities on the mode value of 310 K for the uncorrected graphs or 290 K for the corrected graphs, this could well be a statistical effect, as there are increasingly fewer HII regions as the luminosity increases.

4.2.2. The correlation between $L(\mathrm{H}\alpha)$ and L(IRAC)

The other main result presented here is the strong positive correlation between the luminosity in Hα and the IR luminosity as measured with IRAC. In Fig. 8 we have plotted these quantities against one another. The linear relationship is strong, with a rank correlation coefficient of 0.79 (see Press et al. 1986), and the two-sided significance level of its deviation from zero is 7.73×10^{-18}. In Table 3 we show the values of the slopes and the intercept constants, using two versions of weighting: uniform weighting (weighting factor = 1) and statistical fluctuation

Table 2. Estimated T_{col} and L(IRAC) of selected K-HII regions (with corrections).

K-HII ID	T_{col} (K)	δT_{col} (K)	L(IRAC) (erg/s)	δL(IRAC) (erg/s)
0047	289.0	6.0	8.6e+39	1.7e+39
0091	329.0	4.0	1.1e+40	1.5e+39
0182	298.0	3.0	4.0e+40	4.8e+39
0196	283.0	3.0	5.3e+40	6.5e+39
0238	292.0	2.0	1.9e+41	1.8e+40
0352	292.0	4.0	2.7e+40	3.8e+39
0396	304.0	2.0	9.1e+40	9.1e+39
0462	291.0	2.0	1.5e+41	1.5e+40
0493	299.0	2.0	7.6e+40	8.1e+39
0504	289.0	2.0	1.0e+41	1.0e+40
0517	253.0	5.0	5.3e+40	1.0e+40
0546	314.0	4.0	1.8e+40	2.7e+39
0585	300.0	1.0	2.6e+41	2.2e+40
0623	286.0	3.0	6.0e+40	7.1e+39
0639	303.0	2.0	1.1e+41	1.0e+40
0651	299.0	1.0	3.0e+41	2.5e+40
0681	276.0	3.0	5.8e+40	7.5e+39
0702	298.0	2.0	1.2e+41	1.2e+40
0733	292.0	3.0	3.1e+40	4.1e+39
0737	294.0	1.0	2.3e+41	2.1e+40
0740	293.0	2.0	2.6e+41	2.3e+40
0763	323.0	2.0	7.1e+40	6.8e+39
0788	275.0	4.0	3.4e+40	5.0e+39
0818	295.0	2.0	8.6e+40	8.8e+39
0846	302.0	2.0	1.4e+41	1.3e+40
0870	301.0	4.0	2.0e+40	2.9e+39
0885	311.0	4.0	1.7e+40	2.4e+39
0921	310.0	1.0	5.3e+41	4.3e+40
0945	283.0	4.0	2.1e+40	3.4e+39
0953	301.0	1.0	4.7e+41	3.8e+40
0963	293.0	1.0	5.9e+41	4.8e+40
0991	300.0	3.0	4.5e+40	5.2e+39
1008	282.0	9.0	4.2e+39	1.2e+39
1026	294.0	2.0	7.1e+40	7.8e+39
1033	289.0	5.0	1.3e+40	2.3e+39
1039	284.0	2.0	6.5e+40	7.7e+39
1085	290.0	3.0	3.6e+40	4.8e+39
1092	304.0	2.0	4.2e+40	5.0e+39
1149	311.0	2.0	7.5e+40	7.4e+39
1158	286.0	3.0	5.3e+40	6.8e+39
1162	280.0	3.0	6.2e+40	7.6e+39
1166	320.0	2.0	3.8e+40	4.2e+39
1195	264.0	6.0	2.3e+40	5.2e+39
1222	290.0	4.0	3.2e+40	4.6e+39
1244	296.0	2.0	1.2e+41	1.2e+40
1247	292.0	4.0	3.1e+40	4.4e+39
1264	363.0	4.0	1.0e+40	1.4e+39
1300	317.0	3.0	2.9e+40	3.4e+39
1324	297.0	3.0	3.0e+40	3.9e+39
1343	302.0	2.0	1.4e+41	1.3e+40
1349	318.0	2.0	2.6e+40	3.3e+39
1368	304.0	2.0	1.0e+41	1.0e+40
1369	275.0	3.0	4.0e+40	5.7e+39
1377	279.0	3.0	6.4e+40	7.7e+39
1394	293.0	2.0	9.8e+40	1.1e+40
1409	299.0	2.0	7.5e+40	8.1e+39
1416	297.0	1.0	2.7e+41	2.3e+40
1419	332.0	2.0	6.5e+40	6.4e+39
1433	294.0	2.0	5.6e+40	6.5e+39
1454	287.0	2.0	9.5e+40	1.1e+40
1511	319.0	2.0	2.3e+40	2.9e+39
1566	304.0	3.0	5.0e+40	5.7e+39
1567	295.0	4.0	2.5e+40	3.4e+39
1574	318.0	2.0	4.4e+40	4.8e+39

Table 2. continued.

K-HII ID	T_{col} (K)	δT_{col} (K)	L(IRAC) (erg/s)	δL(IRAC) (erg/s)
1610	284.0	4.0	3.1e+40	4.3e+39
1625	265.0	3.0	6.1e+40	8.3e+39
1650	269.0	3.0	8.5e+40	1.1e+40
1667	295.0	2.0	1.6e+41	1.5e+40
1674	298.0	2.0	6.3e+40	7.0e+39
1708	302.0	2.0	6.3e+40	6.7e+39
1772	287.0	3.0	4.0e+40	5.2e+39
1810	304.0	2.0	1.7e+41	1.5e+40
1837	302.0	2.0	1.8e+41	1.6e+40
1874	283.0	3.0	5.7e+40	7.0e+39
1882	307.0	2.0	9.6e+40	9.1e+39
1891	276.0	4.0	3.5e+40	5.1e+39
1922	295.0	5.0	1.1e+40	2.0e+39
1928	289.0	2.0	9.5e+40	1.0e+40

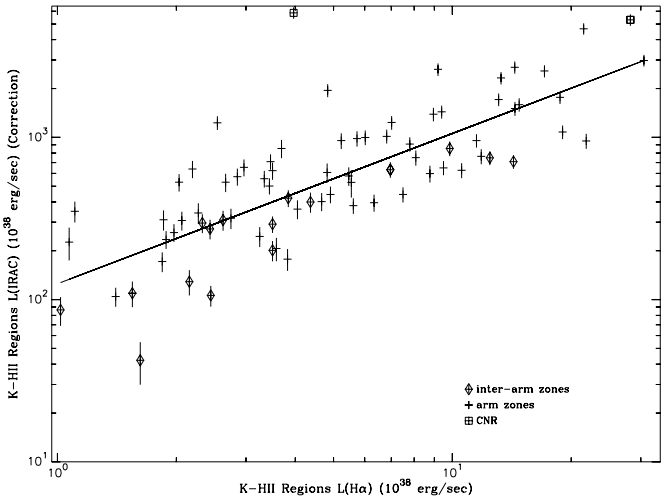

Fig. 8. Using colour+aperture-corrected fluxes to derive L(IRAC) v. Hα luminosity L(Hα) for our HII region sample.

weighting (weighting factor = $1/y_i$, where y_i is one of the dependent variables, see Bevington 1969). It is of interest that the slopes of both graphs are unity within the measurement errors. The IR and Hα luminosities are clearly linearly proportional for our sample. This proportionality holds for regions within the arms and in the interarm zone, with an rms scatter of around 0.2 dex. One of the circumnuclear HII regions lies well above the general trend, indicating, in all probability, enhanced conversion of higher energy photons to IR owning to a much higher dust concentration.

4.3. Radial distribution of colour temperatures $T_{col(IRAC)}$ in the disc of M100

Most of the regions (60 out of 78) measured here are in the spiral arms of the galaxy, sixteen are in the interarm zones, and only two are in the circumnuclear region. We have plotted the values of the colour temperature, $T_{col(IRAC)}$, in the regions against galactocentric radius, in Fig. 9, and it is clear that there is no trend at all with radius. We note this because the electron temperatures in HII regions have been measured to increase with galactocentric radius. This was first found within the Galaxy, using radio recombination lines, by Churchwell & Walmsley (1975), and confirmed by Talent & Dufour (1979). A refined set of observations by Afflerbach et al. (1996) found that if D_G is the galactocentric radius of an HII region in the disc of the Galaxy, its electron

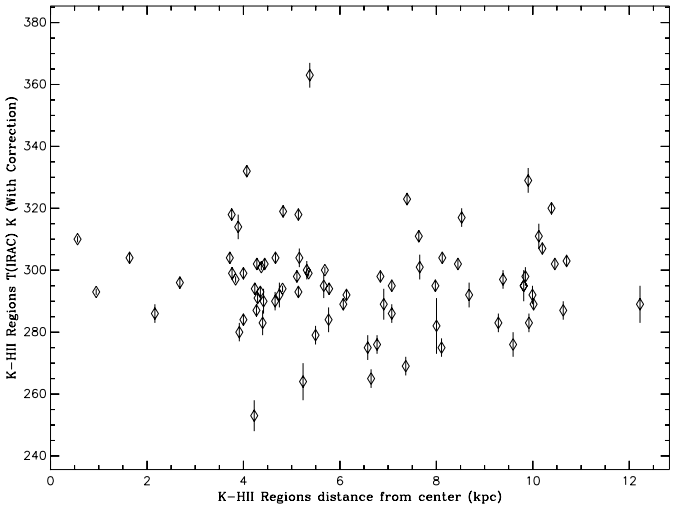

Fig. 9. The radial distribution of colour temperature, $T_{col(IRAC)}$ for the K-HII regions in the disc of M100.

temperature, T_e, can be expressed as $T_e = 5537(\pm387) + 320D_G$ where T_e is in K and D_G in kpc. The important point here is the gradient, which has more recently been determined by Quireza et al. (2006) as 287 (±46) K kpc^{-1}. Although measurements with this degree of accuracy are not generally available for external galaxies, a number of authors have used emission line ratios to measure positive gradients in the electron temperature with increasing galactocentric radius dating from the results of Rayo et al. (1982). Our IR measurements span a reasonably wide range of galactocentric radius so that if there were a significant gradient in the temperature $T_{col(IRAC)}$ we should expect to detect it. It is apparent from Fig. 9 that there is no significant dependence of $T_{col(IRAC)}$ on galactocentric radius, in contrast to the behaviour of the electron temperature.

5. Discussion

5.1. Star formation rate

There is a linear relation with high rank coefficient in the log-log plot between L(IRAC) and L(Hα) (see Table 3). The slope of the relation is indistinguishable from unity, and there is a measurable offset. This linear relation should allow us to use the near-IR luminosity of an HII region as a proxy for Hα when estimating the star formation rates associated with HII regions, so that a good estimate of the star formation rate could be derived by combining near-IR with mid-IR observations.

5.2. Dust emission shells around hot star clusters

It is very interesting to note that there is no correlation between L(Hα) and $T_{col(IRAC)}$, although there is a tendency for the value of the latter to cluster around 300 K for the high-luminosity regions. This could be accounted for in a scenario where the dust in the ISM surrounding an ionizing star cluster is swept out to beyond a radial distance from the cluster, which depends on the cluster luminosity. In any HII region the dust emission would then come from a thick shell whose inner radius is larger the higher the stellar luminosity. A zero-order approximation gives a baseline result for modelling, that the inner radius of the emitting dust shell should vary as $L_c^{1/2}$ where L_c is the luminosity of the cluster. One possible way of approaching this would be to use a stellar wind model of the type first developed by Castor et al. (1975), which has been extended and used by many subsequent

Table 3. The slopes and y-intercepts of L(IRAC) and L(Hα).

Luminosity (log-log scale)	Slope (Statistical fluctuation weighting)	Intercept contant (Statistical fluctuation weighting)	Slope (Uniform wighting)	Intercept contant (Uniform wighting)
L(Hα) and L(IRAC)	(1.02 ± 0.50)	(1.79 ± 0.37)	(0.98 ± 0.09)	(1.84 ± 0.07)
L(Hα) and L(IRAC) (with Corrections)	(0.93 ± 0.53)	(2.10 ± 0.39)	(0.90 ± 0.09)	(2.15 ± 0.07)

authors. It is generally conceded that the driving mechanism for the wind is the radiation field of the star absorbed directly by the atoms of the circumstellar gas. These winds, which for early-type stars imply mass loss rates of order 10^{-6} $M_{\odot}$ yr^{-1} and velocities in the range 1000−2000 km s^{-1}, are a key energy source for the ISM. In addition to the wind we should add the possibility that the major photon fluxes from the OB stars can couple directly to the dust and drive it from proximity to the stars. Another mechanism that might lead to the near invariance of the temperatures we measure could be the phenomenon of dust destruction. A number of mechanisms capable of destroying dust grains can act in the neighbourhood of hot stars, among them sputtering or sublimation. (Morales et al. 2011) invoke dust destruction to explain their observations of dust temperatures around main sequence stars, ranging from B8 to K0. Using IRS/MIPS data from *Spitzer*, in the spectral range from 5 μm to 35 μm they find two distinct dust components with temperatures of ∼190 K and ∼60 K, with little variation along the sequence. They explain the inner warmer dust as due to small grains released from icy planetesimals, released at a temperature horizon that varies according to the stellar type, yielding an approximately invariant temperature. It is also interesting to note that one proposed heating mechanism for small grains is stochastic heating (Draine & Li 2007), in which a grain is heated by absorption of a single photon. This form of heating implies that the temperatures of the grains do not respond in the same way as they would if they were in thermodynamic equilibrium, so that their mean temperature does not depend on the luminosities of the stars supplying the photons, and depends only slightly on the temperatures of those stars. Although we have outlined here some conceptual models and mechanisms that could, in principle, account for our results, our aim is to present the overview and the key initial results of the new observational studies, and although the models demand detailed exploration, this is beyond the scope of our work in the present article. We intend to turn our attention to them in a future article, based not only on these results but on more extensive statistical/observational studies now under way.

5.3. The origin of the 3.6 μm excess

The origin of the infrared emission in the IRAC bands is thermal emission from heated dust. However, the three longer wavelength bands can be reasonably well fitted by a single black body curve, while the 3.6 μm emission is clearly in excess of the flux extrapolated to shorter wavelengths from this curve. Following what is by now a very extensive literature on the subject, we identify this excess as an emission feature from polycyclic aromatic hydrocarbon molecules, commonly referred to by the initials PAH. They have been attributed to the C-C and C-H stretching and bending vibrations in the PAH molecules (Puget & Léger 1989), while an alternative model, proposed by Duley & Williams (1988) is that they are due to hydrogenated amorphous graphite particles. They have been observed systematically in many types of interstellar IR sources: HII regions, planetary nebulae, and reflection nebulae around early-type stars (see Glass 1999, p. 102). They have also been observed in nearby infrared galaxies, (see e.g., Imanishi et al. 2006, 2008), to choose a couple of examples from numerous published works. While a series of bands in the near-IR appear in a wide variety of dusty interstellar environments and they are now conventionally referred to as PAH features, and although we feel safe in attributing the 3.6 μm excess observed in all the K-HII regions of M100 to a PAH feature, this does not imply that the details of the origin of the feature are fully understood.

6. Summary

We have analysed the near-IR emission from a set of the most luminous HII regions in M100 (referred to here as K-HII regions) as measured from *Spitzer* with IRAC in the four detection bands of the instrument, with the following results:

(a) With a chi-squared fitting technique, we could find very reasonable single-temperature black body fits to the emission from the 4.5 μm, 5.8 μm, and 8.0 μm bands, giving values for the colour temperature of the dust $T_{\rm col(IRAC)}$ in the range 250 K−350 K. The difference between the colour+aperture-corrected and the uncorrected temperatures is only some 20 K, and based on this initial study, we can see that colour+aperture correction produces a barely statistically significant difference both to the temperatures and the luminosities obtained.

(b) There is a clear excess in the 3.6 μm band for all the regions, which we attribute to PAH emission.

(c) There is a strong correlation between the luminosity, L(Hα), in the Hα emission line and L(IRAC), the total near-IR luminosity for the regions measured. This could be useful. Calibrating the L(Hα) – L(IRAC) relation and combining the IRAC luminosity with the mid-IR luminosity should allow a practical derivation of the star formation rates without direct recourse to Hα observations.

(d) However, $T_{\rm col(IRAC)}$ does not show a correlation with the HII region luminosity, a result that is less intuitively obvious than the correlation between the two luminosities in (c). This could be explained in a scenario in which the mean distance of the emitting dust from the central star cluster is greater for regions of higher luminosity, which harbour ionizing stars of higher luminosity and temperature. A detailed mechanism for this, which could involve stellar winds sweeping out the dust, and/or ablation of dust particles close to the star cluster, will need further exploration. There is a reduction in the scatter of $T_{\rm col(IRAC)}$ for regions of higher luminosity, but this might be a statistical effect of the decline in the luminosity function.

Acknowledgements. We thank the anonymous referee for the suggestions that helped us to make significant improvements to the article. We also thank Dr. Aigen Li for helpful discussions. This research has made use of the SIMBAD data base, operated at the CDS, Strasbourg, France. The work is based partially on observations made with the *Spitzer* Space Telescope, which is operated by the Jet Propulsion Laboratory, California Institute of Technology, under a contract with NASA. S.J.C. thanks the Instituto de Astrofisica de Canarias for support during a working visit. The research was partly supported by projects P3/86 of the Instituto de Astrofisica de Canarias, and AYA2007-67625-CO2-01 of the Spanish Ministry of Science and Innovations.

References

Afflerbach, A., Churchwell, E., Acord, J. M., et al. 1996, ApJS, 106, 423
Beichman, C. A., Neugebauer, G., Habing, H. J., & Clegg, P. E. 1988, in IRAS Catalog and Altas, Explanatory Supplement (Washington, D.C.: US Government Print Office)
Beckman, J. E., Rozas, M., Zurita, A., Watson, R. A., & Knapen, J. H. 2000, ApJ, 119, 2728
Bevington, P. R. 1969, Data Reduction and Error Analysis for The Physical Sciences (New York: McGraw-Hill)
Bradley, T., Knapen, J. H., Beckman, J. E., & Folkes, S. L. 2006, A&A, 459, L13
Blommaert, J., Siebenmorgen, R., Coulais, A., et al. 2003, in The ISO Camera, ISO Handbook, 2, Ver 2.0 (Noordwijk: ESA)
Castor, J. I., Abbott, D. C., & Klein, R. I. 1975, ApJ, 195, 157
Cepa, J., & Beckman, J. E. 1990, A&AS, 83, 211
Chiosi, C., & Stalio, R. 1981, in Effects of mass loss on stellar evolution; Proc. of the Fifty-ninth Colloq. (Dordrecht: D. Reidel Publishing Co.), Ap&SS, 89
Churchwell, E., & Walmsley, C. M. 1975, A&A, 38, 415
De Vaucouleurs, G., De Vaucouleurs, A., Corwin, H. G., et al. 1991, Third Reference Catalogue of Bright Galaxies (New York: Springer)
Draine, B. T., & Li, A. 2007, ApJ, 657, 810
Duley, W. W., & Williams, D. A. 1988, MNRAS, 231, 969
Elmegreen, D. M., & Elmegree, B. G. 1987, ApJ, 314, 3
Fazio, G. G., Hora, J. L., Allen, L. E., et al. 2004, ApJS 154, 10
Freedman, W. L., Madore, B. F., & Gibson, B. K. 2001, ApJ, 553
Glass, I. S. 1999, Handbook of Infrared Astronomy (Cambridge, UK: Cambridge Univ. Press)
Hodge, P. W. 1976, ApJ, 205, 728
Hodge, P. W. 1987, PASP, 99, 915
Hora, J. L., Fazio, G. G., Willner, S. P., et al. 2000, Proc. SPIE, 4131, 13
Imanishi, M., Dudley, C., & Maloney, P. R. 2006, ApJ, 637, 114
Imanishi, M., Nakagawa, T., Ohyama, Y., et al. 2008, PASJ, 60, 489
Kennicutt, R. C. 1984, ApJ, 205, 728
Kennicutt, R. C. 1992, in Star Formation in Stellar Systems, eds. G. Tenorio-Tagle, M. Prieto, & F. Sanchez (Cambridge: Cambridge Univ. Press), 191
Kennicutt. R. C, Edgar, B. K., & Hodge, P. W. 1989, ApJ, 337, 761
Kennicutt, R. C. Jr., Armus, L., Bendo, G., et al. 2003, PASP, 115, 928
Kessler, M. F., Steinz, J. A., Anderegg, M. E., et al. 1996, A&A 315, L27
Knapen, J. H. 1998, MNRAS, 297, 255 (SIMBAD online catalogue: J/MNRAS/297/255/catalog)
Knapen, J. H., Arnth-Jensen, N., Cepa, J., & Beckman, J. E. 1993, AJ, 106, 56
Knapen, J. H., Beckman, J. E., Shlosman, I., et al. 1995a, ApJ, 443, L73
Knapen, J. H., Beckman, J. E., Heller, C. H., Shlosman, I., & de Jong, R. S. 1995b, ApJ, 454, 623
Knapen, J. H., de Jong, R. S., Stedman, S., & Bramich, D. M. 2003, MNRAS, 344, 527
Knapen, J. H., Stedman, S., Bramich, D. M., Folkes, S. L., & Bradley, T. R. 2004, A&A, 426, 1136 (SIMBAD online catalogue: /pub/cats/VI/112/fits/ at cdsarc.u-strasbg.fr)
Morales, F. Y., Rieke, G. H., Werner, M. W., et al. 2011, ApJ, 730, L79
Press, W. H., Flannery, B. P., Teukolsky, S. A., & Vetterling, W. T. 1986, Numerical Recipes: The Art of Scientific Computing (Cambridge: Cambridge Univ. Press)
Puget, J. L., & Léger, A. 1989, ARA&A, 27, 161
Quireza, C., Rood, R. T., Bania, T. M., Balser, D. S., & Maciel, W. J. 2006, ApJ, 653, 1226
Rayo, J. F., Peimbert, M., & Torres-Peimbert, S. 1982, ApJ, 255,1
Rozas, M., Beckman, J. E., & Knapen, J. H. 1996, A&A, 307, 735
SINGS Team, 2007, SINGS: The Spitzer Infrared Nearby Galaxies Survey: Fifth Data Delivery, User Guide
Spitzer Science Center 2006, Infrared Array Camera Data Handbook
Spitzer Science Center 2007, Spitzer Space Telescope Observers Manual
Spitzer's Science Support Team, Spitzer Science Center 2006, IRAC Pocket Guide v5.0
Talent, D. L., & Dufour, R. J. 1979, ApJ, 233, 888
Tokunaga, A. T., Sellergen, K., Smith, R. G., et al. 1991, ApJ, 380, 452
Werner, M. W., Roellig, T. L., Low, F. J., et al. 2004, ApJS, 154, 1
Zurita, A., Rosas, M., & Beckman, J. E. 2000, A&A, 363, 9